

# Off Zone Center or Indirect Bandgap Like Hole Transport in Heterostructures

Gerhard Klimeck<sup>a</sup>, R. Chris Bowen<sup>a</sup>, and Timothy B. Boykin<sup>b</sup>

<sup>a</sup> Jet Propulsion Laboratory, California Institute of Technology, Pasadena, CA 91109

<sup>b</sup> Dept. of Electrical and Computer Engineering and LICOS, The University of Alabama in Huntsville, Huntsville, AL 35899

January 24, 2001

Unintuitive hole transport phenomena through heterostructures are presented. It is shown that for large bias ranges the majority of carriers travels outside the  $\Gamma$  zone center (i.e. more carriers travel through the structure at an angle than straight through). Strong interaction of heavy-, light- and split-off hole bands due to heterostructure interfaces present in devices such as resonant tunneling diodes, quantum well photodetectors and lasers are shown to be the cause. The result is obtained by careful numerical analysis of the hole transport as a function of the transverse momentum,  $k$ , in a resonant tunneling diode within the framework of a sp3s\* second-nearest neighbor tight binding model. Three independent mechanisms that generate off zone center current flow are explained: 1) non-monotonic (electron-like) hole dispersion, 2) lighter quantum well than emitter effective masses, and 3) strongly momentum dependent quantum well coupling strength due to state anti-crossings. Finally a simulation is compared to experimental data to exemplify the importance of a full numerical transverse momentum integration versus a Tsu-Esaki approximation.  
72.80.Ey, 73.40.Gk, 71.20.-b, 73.20.At

## I. INTRODUCTION

### A. Nanoelectronic Modeling (NEMO)

The quantum mechanical functionality of devices such as resonant tunneling diodes (RTDs), quantum well infrared photodetectors, and quantum well lasers are enabled by material variations on an atomic scale. The creation of these heterostructure devices is realized in a vast design space of material compositions, layer thicknesses and doping profiles. The full experimental exploration of this design space is unfeasible and a reliable design tool is needed.

The Nanoelectronic Modeling tool (NEMO) is one of the first commercial grade attempts for such a modeling tool. NEMO was developed as a general-purpose quantum mechanics-based 1-D device design and analysis tool from 1993-97 by the Central Research Laboratory of Texas Instruments (later Raytheon Systems). Free executables can be requested on the NEMO web site<sup>1</sup>. NEMO enables the fundamentally sound inclusion of the required physics: band-structure, scattering, and charge self-consistency based on the non-equilibrium Green function approach. The theory used in NEMO and in this work is documented in references [ 2–4] while some of the major simulation results are documented in references [ 5–11]. NEMO development is presently continued at the Jet Propulsion Laboratory towards the modeling of light detection and emission devices.

### B. Why Quantum Mechanical Hole Transport ?

Quantum mechanical carrier transport research has focused on pure electron transport since most high-speed quantum devices utilize the high electron mobility in III-V materials. Op-

tical devices, however, typically involve quantum states in the valence bands. We study here the pure hole transport in a hole-doped RTD to begin the study of quantum mechanical electron and hole transport in laser structures.

### C. Approach

Hole states are significantly more complicated than electron states due to the existence of light hole (LH), heavy hole (HH) and split-off (SO) bands in (roughly) the same energy range. These bands are coupled<sup>12–15</sup> due to translational symmetry breaking (spatial material and potential variations) that are inherent in any interesting electronic device and due to spin-orbit coupling. Envelope function representations have been used extensively in much of the published work on hole transport<sup>16–23</sup>. This paper is an extension of previous work by Kiledjian *et al.* who use<sup>24,25</sup> a nearest-neighbor sp3s\* empirical tight-binding basis which includes the spin-orbit interaction to all orders and incorporates wavefunction coupling at interfaces through orbital interactions. To better fit<sup>26,27</sup> the complicated valence band dispersion we include both nearest and 2nd-nearest neighbor interactions<sup>4</sup>. The sp3s\* tight binding parameters used in this work and the corresponding anisotropic masses are published elsewhere<sup>28</sup>. Subband energies and widths are calculated<sup>29</sup> as a function of transverse momentum allowing for a intuitive, yet detailed analysis of hole transport mechanisms.

The work presented here was enabled by the implementation of parallelism<sup>30</sup> in NEMO on simultaneous, various levels: voltage, transverse momentum integration and energy integration. The use of massively parallel computers enabled the thorough exploration<sup>30</sup> of the state space in total energy,  $E$  and transverse momentum,  $k$ , for a significant number of

bias points.

#### D. Overview of the Paper

Sections II and III discuss approximations for calculating current. Section IV introduces the density of states and the transmission coefficient at zero transverse momentum and identifies and labels the quantized states in the RTD. Section V analyzes the transverse momentum dispersion in the RTD and its effects on the transmission coefficient. Section VI converts the energy and momentum dependent transmission coefficients to a momentum dependent current density  $J(k)$ : Failure of the Esaki-Tsu approximation and significant current contributions off zone-center are shown. In Section VII three origins of the off-zone center current flow are identified. One of the off-zone center generating mechanisms is based on the momentum dependence of the resonance widths, which are discussed in more detail in Section VIII. Finally a comparison between theory and experiment is examined in section IX and a plea for the simulation of scattering within a multiband basis is made in Section X.

## II. MOMENTUM DEPENDENT CURRENT DENSITY $J(k)$

Neglecting scattering in the central RTD region one can compute<sup>2,8,5</sup> the coherent current using an expression of the form

$$J \propto \int dE \int dk k T(E, k) (f_L(E) - f_R(E)) \quad (1)$$

$$= \int dE \int dk k J(E, k) \quad (2)$$

where  $k$  is the electron momentum transverse to the transport direction normalized to the unit cell  $a$  by  $\frac{\pi}{a}$ ,  $E$  is the total energy,  $T$  the transmission coefficient, and  $f_{L/R}$  the Fermi function in the left/right contact. The dependence on the momentum angle<sup>31</sup> can be shown to be weak<sup>28</sup>.

A transmission coefficient  $T(E, k = \text{const})$  as a function of energy may be expensive to compute<sup>30</sup>, since it may contain sharp resonances ( $10^{-9} - 10^{-3} \text{ eV}$ ) that have to be resolved well in an energy range of typically  $1 \text{ eV}$ . During the NEMO project algorithms that locate<sup>29</sup> and resolve<sup>32</sup> the resonances expedite the computation of  $T(E, k = \text{const})$ . The Hamiltonian matrix elements in the device excluding the boundary conditions depend in a non-trivial form on the transverse momentum, while the energy dependence is strictly linear. It is therefore convenient for numerical reasons to reverse the order of integration in Eq. 2, perform the simple Hamiltonian construction as a function of  $E$  on the inner loop, and to define an intermediate quantity  $J(k)$  as follows:

$$J(k) = \int dE J(E, k) \quad (3)$$

$$\text{such that } J \propto \int dk k J(k) \quad (4)$$

For electron transport it can be shown<sup>28</sup> that  $J(k)$  typically varies smoothly with  $k$  which reduces the number of  $k$  points needed to resolve  $J(k)$ .

This quantity  $J(k)$  is not only numerically convenient, but it also bears physical insight as to “where” the carrier transport occurs in  $k$ -space. It can be shown analytically<sup>28</sup> that for an electron RTD the function  $J(k)$  is peaked at  $k = 0$  and monotonically decreasing with  $k$ . This behavior indicates that the dominant current contribution arises from carriers at the Brillouin zone center  $\Gamma$ . For holes, however, it will be shown that  $J(k)$  can exhibit sharply peaked features *outside* the Brillouin zone center  $\Gamma$  ( $k_{max} > 0$ ). This indicates that more holes traverse the structure at an angle than straight through the heterointerfaces. This is one of the central results of this paper.

## III. TSU-ESAKI FORMULA

One common approach in reducing the required CPU time<sup>30</sup> needed to compute an I-V characteristic is the assumption of parabolic transverse subbands such that the transmission coefficient has an analytic, parabolic transverse momentum dependence:  $T(E, k) = T(E - \hbar^2 k^2 / 2m^*, k = 0)$ . Under this assumption the transverse momentum integration in Eq. 1 can be carried out analytically to result in the so-called Tsu-Esaki<sup>33</sup> formula:

$$J \propto \rho_{2D} \int dE T(E, k = 0) \ln \left( \frac{1 + e^{(E_F - E)/kT}}{1 + e^{(E_F - E - qV)/kT}} \right) \quad (5)$$

where  $T$  is the temperature and  $E_F$  the Fermi energy in the emitter.

The Tsu-Esaki 1-D integration formula is capable of providing qualitatively correct results for electron devices<sup>34</sup>. For hole transport, however, this paper will underline that the analytical Tsu-Esaki integration over the transverse momentum becomes completely invalid<sup>24,25</sup>.

## IV. SPECTRAL QUANTITIES: DENSITY OF STATES, TRANSMISSION, AND SUBBANDS

The model RTD considered here consists of 10 monolayer (ml) AlAs barriers with a 20 ml GaAs well. To avoid complications due to triangular notch states<sup>5,34</sup> outside the RTD a linear potential drop is applied<sup>35</sup>. A degenerate hole Fermi level of  $8.4 \text{ meV}$  is assumed corresponding to a doping of  $10^{18} \text{ cm}^{-3}$ .

Figure 1a) shows the zero bias density of states and transmission coefficients computed with the sp3s\* second nearest neighbor tight binding model. The density of states shows the nodal structure of the central RTD resonances. Three sets of nodes, HH1-5, LH1-4, and SO1 can be identified with the increasing number of lobes with increasing hole energy. Each of the resonances corresponds to a peak in the transmission curve (Figure 1b). The HH mass is significantly larger than the LH

mass resulting in a smaller energy separation between the confined states<sup>36</sup>. The barriers are much more opaque for HH than for LH resulting in much stronger confinement<sup>37</sup>. This stronger confinement reveals itself in a significantly smaller resonance width. Indeed the NEMO resonance finder<sup>29</sup> indicates that the LH ground state is over three orders of magnitude wider than the HH ground state as indicated in the caption of Figure 1.

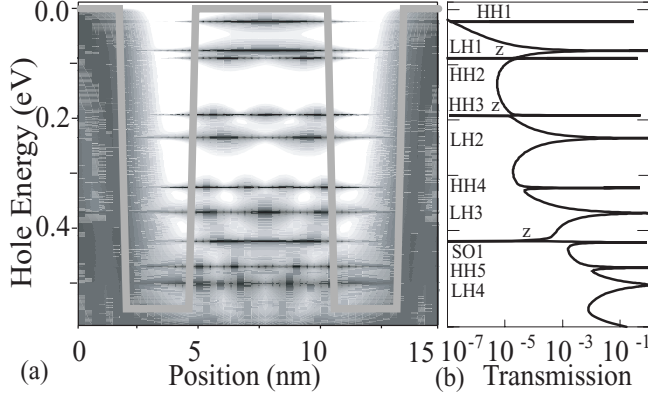


FIG. 1. Density of states (a) and transmission (b) computed in the sp3s\* model. Resonance linewidths are  $HH1-5$  :  $1.4 \times 10^{-5}$ ,  $4.5 \times 10^{-4}$ ,  $1.8 \times 10^{-3}$ ,  $1.2 \times 10^{-2}$ ,  $2.8 \times 10^0$  meV, and  $LH1-4$  :  $5.4 \times 10^{-2}$ ,  $1.7 \times 10^0$ ,  $4.6 \times 10^0$ ,  $1.9 \times 10^1$  meV, and  $SO1$  :  $8.2 \times 10^{-2}$  meV. Transmission zeros are indicated with z.

Note that the transmission coefficient does not reach unity for several of the resonance states due to the coupling of the states even at zero bias. An independent single band model would provide unity transmission coefficients on resonance<sup>28</sup>. Furthermore there are some transmission zeros evident in the multiband case<sup>24,21,19</sup> (labeled z in Fig. 1). These features are all characteristics of the Fano lineshape which occurs when a bound state is coupled to a continuum<sup>38</sup>. In the case of hole transport *all* the resonances are of the Fano type. Transmission zeros occur for isolated Fano resonances. The zeros move off the real axis in conjugate pairs for overlapped Fano resonances<sup>29</sup>. This explains the lack of transmission zeros for the light hole resonances. Note that unlike the  $k \cdot p$  model<sup>21</sup> the sp3s\* model couples the LH, HH, and SO bands for  $k = 0$  even for zero bias due to symmetry breaking and proper inclusion of the spin-orbit interaction.

## V. TRANSVERSE MOMENTUM DEPENDENT TRANSMISSION COEFFICIENTS

The previous section discussed the coupled multiband transmission coefficient for zero transverse momentum. The coupling of the bands resulted in non-unity transmission coefficients and Fano resonances. Band anisotropy and band coupling results<sup>25,28</sup> in a rather peculiar transverse energy dispersion. The transverse hole dispersion depends on the details of the resonant tunneling diode such as well and barrier thicknesses. Figure 2b) shows the hole dispersion for the

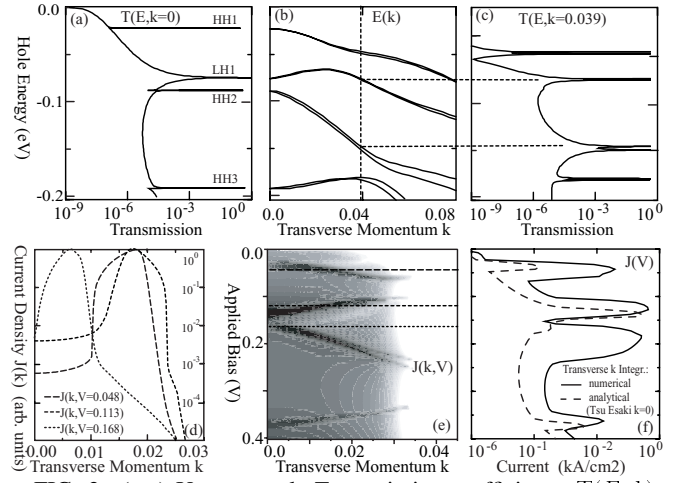


FIG. 2. (a-c) Upper panel: Transmission coefficients,  $T(E, k)$ , and transverse momentum dispersion  $E(k)$  at zero bias. (a)  $T(E, k = 0)$  (compare to Fig. 1b in a smaller energy range), (b)  $E(k)$ , the dispersion is strongly non-parabolic. (c)  $T(E, k = 0.039)$ , transmission is clearly not just an energy shifted version of the transmission coefficient of (a). Spectral features are significantly altered. (d) Current density integrand  $J(k)$  (Eq. 3) on a logarithmic scale for three different applied voltages: 0.048V, 0.113V, and 0.168V.  $J(k)$  shows peaks off the zone center at  $k > 0$ . (e) Gray-scale log plot of the current density integrand  $J(k, V)$  as a function of transverse momentum and applied bias (dark=high value, light=low value). The horizontal dashed lines correspond to the three cuts along  $k$  shown in (d). (f) Integrated current voltage characteristics. Solid line for complete numerical integration over  $k$ . The dashed line is obtained from Tsu-Esaki approximation and therefore corresponds to a vertical cut<sup>40</sup> through (e) along the  $k = 0$  line.

hole RTD described above at zero bias. Various anticrossings can be traced in the  $E(k)$  diagram which serve as another evidence of the interacting quantum states of the various bands. Such strong interaction suggests that there will be a strong dependence of the transmission coefficients on the transverse momentum<sup>25,28</sup>. This strong dependence is demonstrated for two different momenta,  $k = 0$  and  $k = 0.039$  in Figures 2a) and (c), respectively. The location of the resonance energies in Figure 2c) correspond to the intersection of the dispersion in Figure 2b) with the dashed vertical line at  $k = 0.039$ . The spin splitting<sup>39</sup> in the dispersion of Figure 2c) results in double peaks of the transmission coefficient. Figure 2c) is not merely an energy shifted version of the zero transverse momentum case; in fact it has little resemblance at all. The assumption in the Tsu-Esaki formula derivation of  $T(E, k) = T(E - \hbar^2 k^2 / 2m^*, k = 0)$  breaks down completely for quantized hole states.

The strong transverse momentum dependence in the transmission coefficient shown in Figure 2a-c) will result in an interesting dependence of the current flow distribution in momentum and energy as discussed in the next section.

We have also examined the density of states and the structure of the eigenstates at  $k = 0.039$  corresponding to Figure 2c) and found that the nodal symmetries that are visible

in the density of states shown in Figure 1a) are completely broken. We expect this break in the symmetry to have significant effects on the strength of optical matrix elements and leave further discussion to a later publication.

## VI. CURRENT DENSITY $J(k)$ AND CURRENT-VOLTAGE CHARACTERISTIC

The previous section V showed a rich structure in the transverse hole dispersion and transmission coefficients. In this section the transmission coefficient  $T(E, k)$  is converted into a current density  $J(E, k)$  (Eq. 2) and integrated over energy  $E$  (Eq. 3) to result in the spectral quantity  $J(k)$ . This integration is performed at a temperature of 4.2K in a bias range of 0-0.4V and the resulting spectrum of  $J(k, V)$  is plotted in Figure 2e) on a logarithmic, gray scale. Sharply defined streaks of current flow are visible in the momentum space. The current streaks resemble the transverse subband dispersion if the voltage axis is converted into an energy axis (with a factor of 0.5, due to the linear potential drop). The key information to take from Figure 2e) is to realize that the current density  $J(k)$  has maxima that are *not* at  $k = 0$ . This is shown explicitly by three cuts through the contour plot at constant voltages of 0.048V, 0.113V and 0.168V in Figure 2d). The current density is sharply peaked at a transverse momentum  $k \neq 0$  as shown by the logarithmic scale.

Finally, Figure 2f) shows two current voltage characteristics computed with<sup>41</sup> (solid line, Eq. 4) and without (dashed line, Eq. 5) explicit integration over the transverse momentum on a logarithmic scale. The full integration with the transverse momentum shows a significantly enhanced current flow and current features that do not even show up in the analytic transverse integration. The origin of these additional channels in the current voltage characteristic is depicted in the plots of the current density  $J(k, V)$  of Eq. 3 in Figures 2d,e). The sharp peaks at  $k \neq 0$  are completely ignored in the analytical Tsu-Esaki integration that is based solely on the current density at  $k = 0$ . In fact the dashed line in Figure 2f) can be considered a vertical cut<sup>40</sup> through the contour of Figure 2f) at a constant transverse momentum  $k = 0$ .

Note that the current paths that appear enhanced over the analytical Tsu-Esaki integration appear over wide voltage ranges. One can therefore conclude that the current is dominated by off-zone center flow in these wide voltage ranges. This conclusion can be verified explicitly using a simple analytical expression for the current<sup>28</sup>. The resonant tunneling diode therefore serves as a non-zero momentum filter. Such a filter might be useful for spin injection systems.

Figure 2 represents two of the central results of this paper:

1. The current density  $J(k)$  can be sharply spiked outside the zone center  $\Gamma$  at  $k \neq 0$  indicating that more holes traverse the structure at an angle than straight through, similar to an indirect bandgap material, and

2. to capture this physics one *must* accurately resolve bandstructure and perform an explicit numerical integration<sup>41</sup> over the transverse momentum.

## VII. ORIGIN OF THE OFF-ZONE CENTER CURRENT FLOW IN $J(k)$

The previous section demonstrated numerically that there is a significant off-zone center current flow in hole resonant tunneling diodes for wide voltage ranges. The following three sub sections will provide some physical insight into three (almost) independent mechanisms that can generate this unintuitive phenomenon:

- A non-monotonic dispersion,
- B lighter well than emitter effective mass, and
- C resonance linewidth enhancement at  $k > 0$ .

### A. Off-Zone Center Current Flow due to Non-monotonic Dispersion

The common understanding of resonant tunneling diode transport for electrons is that the crossing of the bottom of the electron dispersion with the Fermi energy in the emitter starts the current flow in the device. With the strongly non-monotonic behavior of the hole dispersion (see for example the LH1 state in Fig. 2b) where the dispersion maximum actually occurs at  $k = k_{max} > 0$ ) one can imagine that the current turn-on can be determined by the crossing of this maximum of the valence band with the Fermi level. One can therefore expect that most of the current flows in a cone with the momentum  $k_{max}$ . Figure 3 verifies this physical argument.

Figure 3a) provides an overview of the energy scales of the subbands that might be involved in hole transport at a bias of 0.113V (compare to Fig. 2b). The emitter valence band edge is set to be the zero energy origin. The emitter hole states are occupied in a narrow energy range below the valence band edge as indicated by the shaded area. The HH1 subband is pulled above the valence band edge and cannot conduct holes. The HH2 subband is too far below the Fermi-sea to conduct. Only the LH1 subband is within reach of the shaded Fermi-sea.

Figure 3b) shows an expanded version of 3a) in the energy range of the Fermi sea of the emitter. Furthermore the Fermi-sea of the emitter is shown in more detail as the HH and LH emitter dispersions are shown filled (with gray areas) up to the Fermi energy. It is important to note that this is a 3-D emitter of holes since we apply no potential drop in the emitter. There is therefore no 2-D band quantization in the emitter.

The  $LH1 \uparrow$  and  $\downarrow$  states<sup>39</sup> are shown in dashed lines. At this particular bias it is found that the  $LH1 \downarrow$  dispersion crosses the Fermi level in a momentum range  $k \in [0.016, 0.033]$ . However the LH emitter can only provide holes in the range of

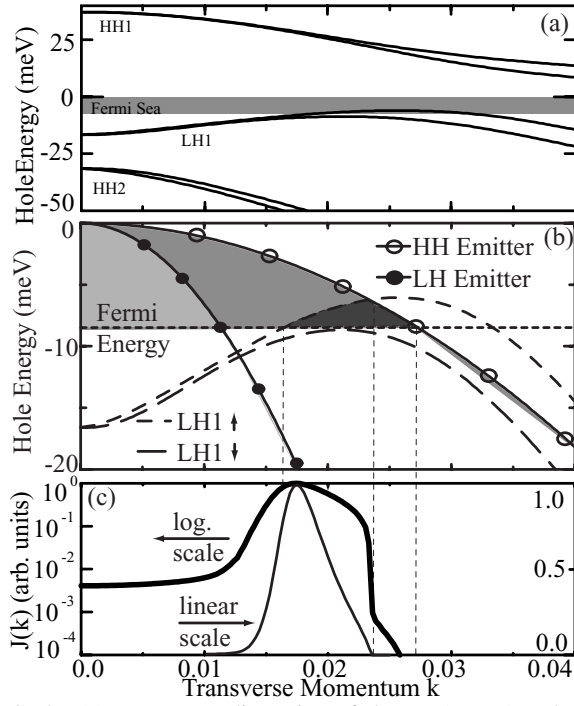


FIG. 3. (a) Transverse dispersion of the HH1, LH1 and HH2 states computed at a bias of 0.113V (0meV is the emitter valence band edge). The gray region indicates the Fermi-sea of holes in the emitter. HH1 and HH2 states are out of the energy range for conduction. (b) Detailed plot of (a) in the energy range of transport.  $LH1 \uparrow\downarrow$  states<sup>39</sup> are shown in dashed lines. The Fermi-sea of the emitter is shown as the HH and LH emitter dispersions (lines with symbols) are shown filled (light gray areas) up to the Fermi energy. Dark gray shading shows the momentum and total energy space over which holes in the emitter can find a matching transverse momentum state in the well to tunnel through. (c) Current density  $J(k)$  on a linear and logarithmic scale. Current turn-on at  $k \approx 0.016$  corresponds to  $LH1 \uparrow$  touching into the Fermi sea. Turn-off corresponds to crossing of  $LH1 \uparrow$  with the HH emitter band at  $k \approx 0.0235$ . Linear scale shows that the current is indeed sharply spiked in  $k$ .

$k \in [0, 0.011]$  and the HH emitter in the range  $k \in [0, 0.0275]$ . There can therefore be no injection of LH states into  $LH1 \downarrow$  and all the carriers must be injected from the HH emitter states in a momentum range of  $k \in [0.016, 0.0275]$ . The dark gray shade indicates the momentum and energy domain out of which holes one could intuitively expect carriers to be injected into the central resonance states.

Figure 3c) shows a linear and log-scale plot of the current density  $J(k)$  at the bias of 0.113V. Indeed we find a sharp current turn-on at  $k \approx 0.016$ . However, the first strong turn-off (visible on a log and linear scale) does not occur at  $k \approx 0.0275$  but occurs at  $k \approx 0.0235$ . This corresponds to the crossing of the  $LH1 \uparrow$  dispersion with the HH emitter dispersion. Beyond that crossing the current can be shown<sup>28</sup> to be carried by the evanescent quantum state deriving from  $LH1 \downarrow$  (Lorentzian tail). The final current turn-off at  $k \approx 0.0275$  of  $LH1 \downarrow$  is only visible on a logarithmic scale (see dashed vertical lines). No

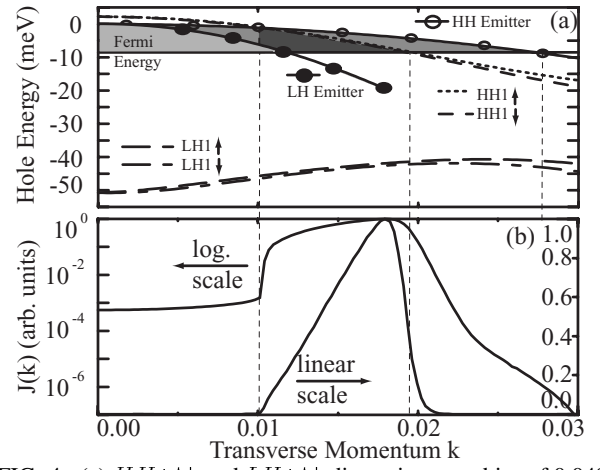


FIG. 4. (a)  $HH1 \uparrow\downarrow$  and  $LH1 \uparrow\downarrow$  dispersions at a bias of 0.048V (dashed lines). The Fermi-sea of the emitter is shown as the HH and LH emitter dispersions (circles) filled (light gray areas) up to the Fermi level. Crossings of  $HH1 \uparrow\downarrow$  and HH emitter dispersion with each other and the Fermi level will result in features of  $J(k)$  in (b) as indicated by vertical lines. LH emitter states do *not* provide any carriers for injection into the quantum well. (b) Numerical  $J(k)$  on a linear and logarithmic scale. Current peak is carried by  $HH1 \uparrow\downarrow$  states as they pass through the emitter injection dispersion and the Fermi-sea.

carriers can be provided to the Lorentzian tail of the  $LH1 \downarrow$  state anymore beyond that point.

Looking at Figure 3 as a whole one can see how the non-monotonic behavior of the hole dispersion can create current features that are sharply spiked in the transverse momentum dependence. The following two sections will describe two other mechanisms that can generate similar spikes in  $J(k)$ .

## B. Off Zone-Center Current Flow due a Lighter Quantum Well than Emitter Effective Mass

The previous section VII A showed that quantum state and emitter dispersion crossings at  $k > 0$  can lead to current turn-ons at  $k > 0$ . Quantum well and emitter dispersion crossings can occur even for simple, almost parabolic, dispersions. In particular this can occur if the effective mass in the quantum well is significantly smaller than in the emitter as shown in Figure 4. Similar to Figure 3 the shape of the current density  $J(k)$  is dominated by the crossings of the quantum well dispersions and the emitter dispersion with each other and the Fermi level in the emitter.

At a bias of 0.048V the main current contribution is due to tunneling through the  $HH1$  states as indicated by the dispersions in Figure 4. The  $HH1$  states have a lighter mass than the bulk  $HH$  states due to an admixture of  $LH$  components. That can cause a crossing of the dispersions as shown in Figure 4 at a momentum of  $k \approx 0.01$ . That crossing corresponds to a turn-on in  $J(k)$  in Figure 4b). That current turn-on is pronounced on a linear as well as a logarithmic scale. The current

turns off at  $k \approx 0.019$  when the  $HH1$  dispersion crosses the Fermi-sea.

Note that the  $HH1$  has a mass that is lighter than the  $HH$  emitter, yet it is still heavier than the  $LH$  emitter. The  $HH1$  state and the  $LH$  emitter dispersion therefore do not cross. Similar to the case at 0.113V in the previous section, we assert<sup>28</sup> here again that the current flowing through the structure is dominated by the  $HH$  emitter injection at bias of 0.048V.

It can be shown analytically<sup>28</sup> that the Lorentzian tails of the  $LH1$  states are responsible for the background current of  $J(k)$  which finally turns off at  $k \approx 0.0275$ . To understand this argument one must realize that the  $HH1$  and  $LH1$  states have dramatically different resonance linewidths (see discussions in Section VIII).

The phenomenon of crossing quantum well and emitter dispersions is not limited to hole transport, but it is indeed quite common for high performance InP-based resonant tunneling diodes<sup>42</sup> where the well might contain InAs, while the emitter is typically InGaAs with a larger effective mass<sup>43,44</sup>. We have seen this effect of non-zone center current flow in direct band gap electron devices in such InGaAs/AlAs/InAs high performance RTD systems.

### C. Off Zone-Center Current Flow due to Resonance Linewidth Modulations

The previous two sections VII A and VII B explained how crossings between emitter dispersion, quantum well dispersion, and emitter Fermi level can lead to current flow that is dominant (sharply peaked) off the zone center in a narrow momentum space. This section will demonstrate how the strong dependence of the resonance linewidth can induce similar off zone center current flow.

The insert in Figure 5c) shows the dispersion of the lowest 8 states at a bias of 0.168V. The shaded area indicates the width of the Fermi-sea in the emitter from which holes can be injected. Only the  $HH2$  states are in the energy range that can provide significant conductance through the structure. Figure 5a) shows the  $HH2$ ,  $HH$  emitter, and  $LH$  emitter dispersions as well as the emitter Fermi level. Given this dispersion one can expect current flow through the  $HH2$  state by injection from either the  $LH$  or  $HH$  states in the emitter. Current flow is expected to cease as a function of transverse momentum as the quantum well and emitter dispersions are crossing the Fermi-sea. Therefore a monotonically decreasing current density could be expected<sup>28</sup>. However, the resonance widths,  $\Gamma$ , of the  $HH2$  states show (Fig. 5c) an increase by over two orders of magnitude in the transverse momentum range of interest. This increase in  $\Gamma$  leads to a dramatic increase in the current density  $J(k)$  as indicated in Figure 5b). The following section VIII will examine the origin of the strong resonance linewidth modulation as a function of transverse momentum in a resonant tunneling structure in more detail.

Unlike the previous two sections where the  $HH$  emitter

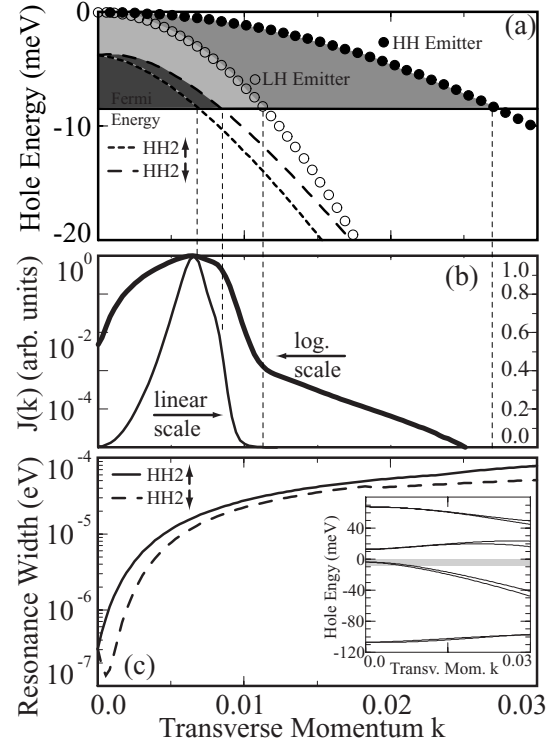


FIG. 5. (a)  $HH2$  dispersion (dashed lines) and  $HH$  and  $LH$  emitter dispersion (circles) at a bias of 0.168V. The Fermi-sea of the emitter is shown as the  $HH$  and  $LH$  emitter dispersions are shown filled (with light gray areas) up to the Fermi level in the emitter. Crossings of the dispersions the Fermi level will result in *turn-off* features of  $J(k)$  in (b) as indicated by vertical lines. (b)  $J(k)$  on a linear and logarithmic scale. The current turn-on is associated with the strong modulation of the resonance width as a function of momentum shown in (c). The inset in (c) is an overview of the quantum well dispersion at this bias. The gray shade indicates the Fermi-sea.

states can be identified as the only current carrying charge injectors one can not make such an assessment in this case. It can be shown analytically<sup>28</sup> that most of the current is injected from the  $LH$  emitter states at this bias.

Note that the turn-on in  $J(k)$  appears smoother on a linear scale compared to the previous cases (see Figs. 3c) and 4b). This is due to fact that the turn-on is generated by the smooth increase in the resonance linewidth  $\Gamma$  and not by a crossing of the various dispersions with a sharply defined Fermi level at a temperature of 4.2K.

## VIII. RESONANCE LINEWIDTH MODULATION

### A. Coupling of $HH1$ and $LH1$

Figure 6 sheds light on the interaction of heavy hole and light hole states and their coupling to the leads as a function of transverse momentum. Figure 6a) shows the subband dispersion previously shown in Figure 2b) in a smaller energy and



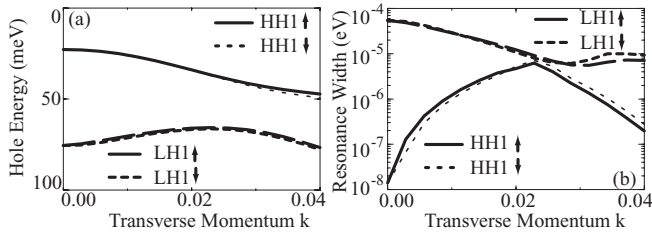


FIG. 6. (a) Same hole dispersion shown in Figure 2b) in a smaller energy and momentum range. Only the four lowest energy hole states are shown including the spin<sup>39</sup>. (b) Resonance linewidth of the states in (a). The HH1 states show a variation of the resonance linewidth of several orders of magnitude as a function of transverse momentum. The LH1 state shows a reduction of resonance width by about an order of magnitude. The resonances interact very strongly at the anticrossing at  $k \approx 0.022$ .

transverse momentum range. Only the four top most states including the spins<sup>39</sup> are depicted.

Figure 6b) shows the associated resonance linewidths<sup>29</sup> as a function of transverse momentum of the first four states. The two highest states (HH1) show the expected (see caption of Fig. 1) narrow line widths of about  $10^{-8}$  eV at zero transverse momentum. The next two states have resonance linewidths of about  $5 \times 10^{-5}$  eV which is indicative of the LH states.

Figure 6a) shows an anti-crossing at a transverse momentum of about 0.022. This anti-crossing has a very dramatic impact on the heavy hole coupling to the leads as indicated by the large increase of the resonance line width by about three orders of magnitude compared to the zero transverse momentum result. Such a large increase in the resonance line width for this particular channel can result in a significant current increase as discussed in Figure 5 in Section VII C. This strong resonance width modulation will only have an impact if there is a significant number of carriers at the transverse momentum of 0.025. This is the case as the Fermi level or the temperature is increased<sup>28</sup> in our RTD.

It is emphasized here that the anti-crossing has dramatic effects on the resonance linewidths of the involved states over several orders of magnitude, while the resonance state energies are distorted only by a few meV.

### B. Coupling between LH1 and HH2

The previous Section VII A illustrated how the HH1 and LH1 state interaction created a significant resonance linewidth modulation at the anti-crossing at  $k \approx 0.022$ . Section VII C argued with Figure 5 that the strong resonance linewidth modulation of HH2 is responsible for the off-zone current flow at a bias of 0.168V. Here we try to explain this linewidth modulation.

In Figure 1 the sequence of the lowest hole quantum states in the resonant tunneling diode was identified as HH1, LH1, and HH2 by the nodal symmetry (1, 1, and 2 lobes) in the

density of states (Fig. 1a) and the widths (narrow, wide, narrow) of the transmission resonances (Fig. 1b).

Using Figure 2b), however, one can argue that the third state (labeled HH2) has actually the dispersion of a quantized LH state for  $k > 0$  (large slope). Using a few other diagrams<sup>28</sup> that quantize the anisotropic bulk HH band it can also be shown that the second state labeled here as LH1 has actually HH qualities for  $k > 0$ . It is argued here that there is actually an anti-crossing of LH1 and HH2 at  $k \approx 0$ . At  $k = 0$  the sequence appears to be HH1, LH1, HH2, while for  $k > 0$  the sequence appears as HH1, HH2, LH1. Correspondingly one can expect the resonance linewidth of the third state to increase significantly with transverse momentum as it changes its character from HH2 to LH1. That is exactly what is shown in Figure 5b).

## IX. COMPARISON AGAINST EXPERIMENT

Hole resonant tunneling diodes have been investigated experimentally in some detail<sup>45</sup>. Negative differential resistance and effects due to charge accumulation in the central RTD and emitter region have been observed in a variety of different structures.

Hayden *et al.* studied<sup>45</sup> the effect of charge accumulation and intrinsic bi-stability in an asymmetric RTD. Their structure is described<sup>45</sup> as "a 4.2-nm GaAs quantum well formed between two AlAs tunnel barriers of thickness 4.5 and 5.7 nm. Undoped spacer layers of thickness 5.1 nm separate the two tunnel barriers from Be-doped contact layers in which the doping is graded from  $5 \times 10^{17} \text{ cm}^{-3}$  to  $2 \times 10^{18} \text{ cm}^{-3}$  over a distance of 200nm." The mesa size is assumed<sup>46</sup> to be  $100 \mu\text{m}$ . Figure 7 shows the charge-empty forward bias direction current voltage characteristic taken from Figure 2 of reference [45] in a solid line. Without the charge accumulation in the central RTD we can avoid computing the full Hartree charge selfconsistently and use a semi-classical potential profile and obtain reasonable<sup>5,8</sup> results.

We entered the structure as described by Hayden<sup>45,46</sup> into NEMO, chose a optical relaxation rate of 24meV in the contact regions<sup>5</sup>, and used the same second nearest neighbor sp3s\* model as in the rest of this paper. In Figure 7 two simulation results, 1) full numerical transverse momentum integration, and 2) analytical transverse momentum integration, are compared to experimental data. The simulation results have to be scaled down<sup>47</sup> by a factor of 20.0 to be compared to the experimental data on a linear scale.

The main point of this section is not to achieve a perfect fit<sup>47</sup> but it is to highlight the need for a full numerical transverse momentum integration. Similar to the current voltage characteristic shown in Figure 2f) one can see here again that the analytical Tsu-Esaki integration misses a current carrying channel (HH2) completely.

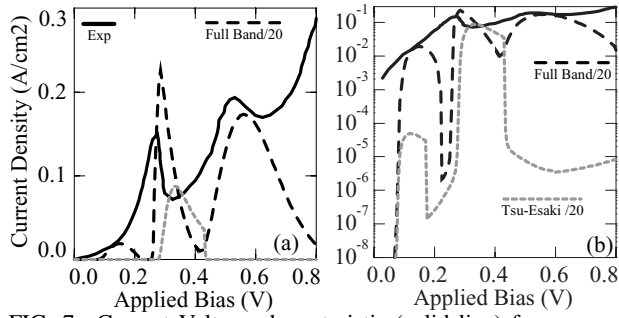


FIG. 7. Current Voltage characteristic (solid line) for an asymmetric hole RTD from reference [ 45] compared to our simulation results with full numerical integration (dashed line) and with analytical (Tsu-Esaki) integration (gray dotted line) scaled down<sup>47</sup> by an arbitrary factor of 20.0 (dashed line). (a) linear scale. (b) log scale. The Tsu-Esaki approximation completely misses the third conduction peak similar to Figure 2f) and underestimates the first one severely. The deviation between the two simulated results indicates that most of the current flows off-zone center.

## X. A NEED FOR MULTIBAND-BASIS SIMULATIONS INCLUDING SCATTERING

The comparison in Figure 7 shows that the simulation is clearly deviating from the experimental results in the valley currents. We attribute this to the lack of incoherent scattering in the central RTD in our simulation. At this stage NEMO can only simulate interface roughness, polar optical phonon, acoustic phonon and alloy disorder scattering in a single band model<sup>9–11</sup>. Such a single band model is, however, incapable to incorporate the HH, LH and SO hole band interactions which are the first order effects that establish the coherent channels through the central RTD.

For pure electron transport in RTD's it has been shown<sup>9–11</sup> that at low temperatures bandstructure effects are negligible and scattering processes due optical phonons and interface roughness are dominant. As an overall conclusion to the comparison to experimental data we submit that at low temperatures the combined inclusion of incoherent scattering and the full bandstructure with full numerical transverse momentum integration is essential to completely model the current flow through a hole RTD.

## XI. SUMMARY

This work demonstrates two key findings: 1) HH and LH interaction is shown to be strong enough to result in dominant current flow off the  $\Gamma$  zone center, and 2) proper modeling and explicit inclusion of the transverse momentum in the current integration is needed. Three mechanisms that generate off zone center current flow are shown: 1) non-monotonic (electron-like) hole dispersion, 2) different quantum well and emitter effective masses, and 3) momentum dependent quantum well coupling strength. From a comparison of a simulation to experimental data it is suggested that the inclusion of

full bandstructure as well as incoherent scattering is needed to completely model current-voltage characteristics in RTD's.

## XII. ACKNOWLEDGEMENTS

The work described in this publication was carried out at the Jet Propulsion Laboratory, California Institute of Technology under a contract with the National Aeronautics and Space Administration. The supercomputer used in this investigation was provided by funding from the NASA Offices of Earth Science, Aeronautics, and Space Science. Part of the research reported here was performed using HP SPP-2000 operated by the Center for Advanced Computing Research at Caltech; access to this facility was provided by Caltech.

G.K. and R.C.B. would like to acknowledge the careful review of an early manuscript and valuable comments by Marc Cahay. G.K. acknowledges the careful review of the final manuscript by Fabiano Oyafuso.

- <sup>1</sup> See <http://hpc.jpl.nasa.gov/PEP/gekco/nemo> or search for NEMO on <http://www.raytheon.com>.
- <sup>2</sup> R. Lake, G. Klimeck, R. C. Bowen, and D. Jovanovic, J. Appl. Phys. **81**, 7845 (1997).
- <sup>3</sup> R. Lake, G. Klimeck, R. Bowen, D. Jovanovic, and D. Blanks, Phys. Stat. Sol. (b) **204**, 354 (1997).
- <sup>4</sup> T. B. Boykin, L. J. Gamble, G. Klimeck, and R. C. Bowen, Physical Review B **59**, 7301 (1999).
- <sup>5</sup> G. Klimeck, R. Lake, R. C. Bowen, W. R. Frensley, and T. Moise, Appl. Phys. Lett. **67**, 2539 (1995).
- <sup>6</sup> R. Lake, G. Klimeck, R. C. Bowen, C. Fernando, D. Jovanovic, D. Blanks, T. S. Moise, Y. C. Kao, M. Leng and W. R. Frensley in the 1996 54th Annual Device Research Conference Digest, (IEEE, NJ, 1996), p. 174.
- <sup>7</sup> G. Klimeck, T. B. Boykin, R. C. Bowen, R. Lake, D. Blanks, T. S. Moise, Y. C. Kao, and W. R. Frensley in the 1997 55th Annual Device Research Conference Digest, (IEEE, NJ, 1997), p. 92.
- <sup>8</sup> R. C. Bowen, G. Klimeck, R. K. Lake, W. R. Frensley, and T. Moise, J. Appl. Phys **81**, 3207 (1997).
- <sup>9</sup> R. Lake, G. Klimeck, R. C. Bowen, C. Fernando, M. Leng, T. Moise, and Y. C. Kao, Superlatt. and Microstruct. **20**, 279 (1996).
- <sup>10</sup> R. Lake, G. Klimeck, and D. K. Blanks, Semicond. Sci. Technol. **13**, A163 (1998).
- <sup>11</sup> G. Klimeck, R. Lake, and D. K. Blanks, Phys. Rev. B. **58**, 7279 (1998).
- <sup>12</sup> E. E. Mendez, W. I. Wang, B. Ricco, and L. Esaki, Applied Physics Letters **47**, 415 (1985).
- <sup>13</sup> R. K. Hayden, D. K. Maude, L. Eaves, E. C. Valadares, M. Henini, F. W. Sheard, O. H. Hughes, J. C. Portal, and L. Cury, Physical Review Letters **66**, 1749 (1991).
- <sup>14</sup> J. A. Kash, M. Zachau, M. A. Tischler, and U. Ekenberg, Physical Review Letters **69**, 2260 (1992).



- <sup>15</sup> W.-C. Tan, J. C. Inkson, and G. P. Srivastava, *Physical Review B* **54**, 14623 (1996).
- <sup>16</sup> J. M. Luttinger and W. Kohn, *Physical Review* **97**, 869 (1955).
- <sup>17</sup> M. Burt, *Semicond. Sci. Technol.* **3**, 739 (1988).
- <sup>18</sup> B. Foreman, *Physical Review Letters* **81**, 425 (1998).
- <sup>19</sup> S. Ekbote, M. Cahay, and K. Roenker, *Physical Review B* **58**, 16315 (1998).
- <sup>20</sup> S. Ekbote, M. Cahay, and K. Roenker, *Journal of Applied Physics* **87**, 1467 (2000).
- <sup>21</sup> C. Y.-P. Chao and S. L. Chuang, *Physical Review B* **43**, 7027 (1991).
- <sup>22</sup> Y. X. Liu, R. R. Marquardt, D. Z.-Y. Ting, and T. C. McGill, *Physical Review B* **55**, 7073 (1991).
- <sup>23</sup> J. X. Zhu, Z. D. Wang, and C. D. Gong, *Solid State Communications* **101**, 257 (1997).
- <sup>24</sup> M. S. Kiledjian, J. N. Schulman, K. L. Wang, and K. V. Rousseau, *Physical Review B* **46**, 16012 (1992).
- <sup>25</sup> M. S. Kiledjian, J. N. Schulman, K. L. Wang, and K. V. Rousseau, *Surface Science* **267**, 405 (1992).
- <sup>26</sup> G. Klimeck, R. C. Bowen, T. B. Boykin, C. Salazar-Lazaro, T. A. Cwik, and A. Stoica, *Superl. and Microstr.* **27**, 77 (2000).
- <sup>27</sup> G. Klimeck, R. C. Bowen, T. B. Boykin, and T. A. Cwik, *Superl. and Microstr.* **27**, 519 (2000).
- <sup>28</sup> Gerhard Klimeck, R. Chris Bowen and Timothy B. Boykin, accepted in *Superlattices and Microstructures* (2001).
- <sup>29</sup> R. C. Bowen, W. R. Frensley, G. Klimeck, and R. K. Lake, *Phys. Rev. B* **52**, 2754 (1995).
- <sup>30</sup> For the simulations presented in this work parallelization was utilized in the integration over the independent momenta  $k$ . Typically 150 points were used for the momentum resolution, while the energy grid resolution may vary adaptively from a few hundred nodes to several thousand nodes depending on the number of resonances in the energy range of interest. The load on 16 or 32 CPUs was balanced in a master-slave approach due to the variability in the execution time of each energy integration. The simulations were run on a 32 CPU Beowulf system based on 450MHz Pentium III, on a SGI Origin 2000, and HP SPP-2000. The final runs that resolve several hundred bias points took about a week to run on our dedicated Beowulf system. The Tsu-Esaki formula (Eq. 5) is so tempting to be used since it reduces the required CPU time in this case by a factor of 150. A more fine grain parallel integration over energy  $E$  or a more coarse grain parallelism over bias points can be used in NEMO for such a computation where there is no explicit integration over momentum  $k$ .
- <sup>31</sup> In this work we assume cylindrical symmetry and use the transverse momentum in the [100] direction.
- <sup>32</sup> G. Klimeck, R. Lake, R. C. Bowen, C. L. Fernando, and W. R. Frensley, *VLSI Design* **6**, 107 (1998).
- <sup>33</sup> R. Tsu and L. Esaki, *Appl. Phys. Lett.* **22**, 562 (1973).
- <sup>34</sup> The Tsu-Esaki can provide qualitatively correct results for electron devices given the restrictive assumption that subband alignment is *not* the primary transport mechanism<sup>48–50,8</sup>. Technologically relevant RTDs that show negative differential resistance at room temperature all exhibit a triangular emitter well such that there is a large 2-D to 2-D subband tunneling contribution from emitter to central resonance. To achieve quantitative agreement<sup>7,8</sup> between simulation and experimental data for such RTDs full 2-D integrations in energy  $E$  and transverse momentum  $k$  according to Eq. 2 must be performed.
- <sup>35</sup> There is no implicit limitation in NEMO to a linear potential drop. Charge self-consistent simulations of the Hartree and exchange and correlation potential are presented in references [5, 7, 8].
- <sup>36</sup> In an infinite barrier square well of width  $a$  the energy separation is  $\Delta E_{n+1} = E_{n+1} - E_n \propto \hbar^2 \pi^2 / 2ma^2 \propto 1/m$ .
- <sup>37</sup> For a single square barrier of thickness  $d$  the exponential  $e^{-\kappa d}$  decay constant is defined as  $\kappa = \sqrt{2m\Delta E/\hbar^2} \propto \sqrt{m}$ .
- <sup>38</sup> U. Fano, *Physical Review* **124**, 1866 (1961).
- <sup>39</sup> The asymmetry of the applied bias has split the two spin states. Note that there is no magnetic field selection in these simulations. The spin degenerate states at  $k = 0$  are split due to the translational symmetry breaking at  $k > 0$ . We use the notation  $\uparrow, \downarrow$  as a shorthand to identify the two states. Since there is no selecting magnetic field we assume that for example  $LH1 \uparrow$  consists of a linear combination of up and down spins.
- <sup>40</sup>  $J(k = 0)$  scales directly with the total current if the Tsu-Esaki formula is employed (Eq. 5) except for a scaling factor including the 2-D density of states  $\rho_{2D}$ .
- <sup>41</sup> We find good numerical stability in these hole RTDs when about 150  $k$  points are resolving a uniform  $k$ -grid in the range of 0-0.05. This number of  $k$  points could possibly be reduced if an adaptive  $k$ -grid were to be introduced.
- <sup>42</sup> T. S. Moise, Y.-C. Kao, A. J. Katz, T. P. E. Broekaert, and F. G. Celii, *J. Appl. Phys.* **78**, 6305 (1995).
- <sup>43</sup> T. B. Boykin, *Phys. Rev. B* **51**, 4289 (1995).
- <sup>44</sup> J. N. Schulman, *Appl. Phys. Lett.* **72**, 2829 (1998).
- <sup>45</sup> R. K. Hayden, L. Eaves, M. Henini, D. K. Maude, and J. C. Portal, *Phys. Rev. B* **49**, 10745 (1994).
- <sup>46</sup> R. K. Hayden, private communication. The mesa sizes used in the experiment have diameter of  $100\mu m$ .
- <sup>47</sup> While a deviation by a factor of 20 might sound large we point out here that such a deviation is not completely unexpected. We have verified with NEMO that variations of 2-3 monolayers in the barrier thickness and variations in the doping profile detail can result in such current density variations of factors of 20. We feel that such deviations can only be eliminated in a controlled testmatrix<sup>7</sup> of experimental structures where experimental trends can be analyzed in more detail. Such a controlled comparison between experiment and theory or arbitrary adjustments to parameters until a perfect fit is achieved are not the point of this presentation.
- <sup>48</sup> T. B. Boykin, R. E. Carnahan, and R. J. Higgins, *Phys. Rev. B* **48**, 14232 (1993).
- <sup>49</sup> T. B. Boykin, R. E. Carnahan, and K. P. Martin, *Phys. Rev. B* **51**, 2273 (1995).
- <sup>50</sup> T. B. Boykin, *J. Appl. Phys.* **78**, 6818 (1995).